# LETTER

# Ultrafast X-ray probing of water structure below the homogeneous ice nucleation temperature

J. A. Sellberg[1,2], C. Huang[3], T. A. McQueen[1,4], N. D. Loh[5], H. Laksmono[5], D. Schlesinger[2], R. G. Sierra[5], D. Nordlund[3], C. Y. Hampton[5], D. Starodub[5], D. P. DePonte[6,7], M. Beye[1,8], C. Chen[1,4], A. V. Martin[6], A. Barty[6], K. T. Wikfeldt[2], T. M. Weiss[3], C. Caronna[7], J. Feldkamp[7], L. B. Skinner[9], M. M. Seibert[7], M. Messerschmidt[7], G. J. Williams[7], S. Boutet[7], L. G. M. Pettersson[2], M. J. Bogan[5] & A. Nilsson[1,2,3]

**Water has a number of anomalous physical properties, and some of these become drastically enhanced on supercooling below the freezing point. Particular interest has focused on thermodynamic response functions that can be described using a normal component and an anomalous component that seems to diverge at about 228 kelvin (refs 1–3). This has prompted debate about conflicting theories[4–12] that aim to explain many of the anomalous thermodynamic properties of water. One popular theory attributes the divergence to a phase transition between two forms of liquid water occurring in the 'no man's land' that lies below the homogeneous ice nucleation temperature ($T_H$) at approximately 232 kelvin[13] and above about 160 kelvin[14], and where rapid ice crystallization has prevented any measurements of the bulk liquid phase. In fact, the reliable determination of the structure of liquid water typically requires temperatures above about 250 kelvin[2,15]. Water crystallization has been inhibited by using nanoconfinement[16], nanodroplets[17] and association with biomolecules[16] to give liquid samples at temperatures below $T_H$, but such measurements rely on nanoscopic volumes of water where the interaction with the confining surfaces makes the relevance to bulk water unclear[18]. Here we demonstrate that femtosecond X-ray laser pulses can be used to probe the structure of liquid water in micrometre-sized droplets that have been evaporatively cooled[19–21] below $T_H$. We find experimental evidence for the existence of metastable bulk liquid water down to temperatures of $227^{+2}_{-1}$ kelvin in the previously largely unexplored no man's land. We observe a continuous and accelerating increase in structural ordering on supercooling to approximately 229 kelvin, where the number of droplets containing ice crystals increases rapidly. But a few droplets remain liquid for about a millisecond even at this temperature. The hope now is that these observations and our detailed structural data will help identify those theories that best describe and explain the behaviour of water.**

Figure 1a sketches our experimental set-up: in vacuum, a liquid jet[19] generates spatially unconfined droplets of supercooled liquid water, the structure of which is then studied using intense, 50-fs, hard-X-ray laser pulses from the Linac Coherent Light Source (LCLS). A Rayleigh jet[20] produces a continuous, single-file train of water droplets with a uniform diameter of 34 or 37 μm, and a gas dynamic virtual nozzle[21] gives trains of smaller droplets with a diameter of 9 or 12 μm. The droplets cool rapidly through evaporation and reach an average temperature that depends primarily on droplet size and travel time through the vacuum (Supplementary Information, section B.3), which we varied systematically by adjusting the distance between the dispenser nozzle and the X-ray pulse interaction region. Scattering patterns (at least 1,800 per data point; Supplementary Information, section A.1.3) were recorded from individual droplets with a single X-ray pulse over the temperature

ranges of 227–252 K and 233–258 K for the droplets generated by gas dynamic virtual nozzle and Rayleigh jet, respectively. Temperature calibrations were performed using the Knudsen theory of evaporative cooling with a typical absolute uncertainty of ±2 K at the lowest temperatures (Supplementary Information, section B.3.5; Supplementary Tables 5 and 6; and Supplementary Fig. 20); the Knudsen theory was verified through extensive molecular dynamics simulations of droplet cooling (Supplementary Information, section B.2).

Figure 1b shows a typical diffraction pattern of a liquid water droplet with a maximum momentum transfer of $q \approx 3.5$ Å$^{-1}$ at the corners of the detector. The isotropic water diffraction rings uniquely identify the
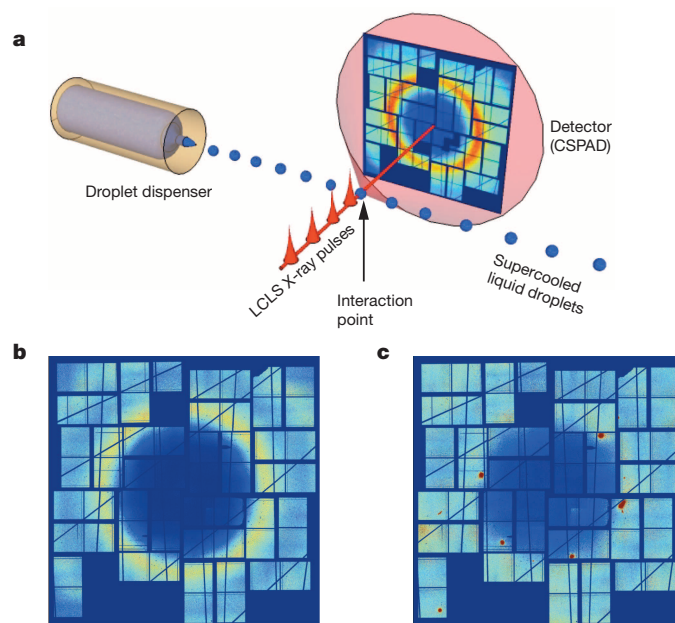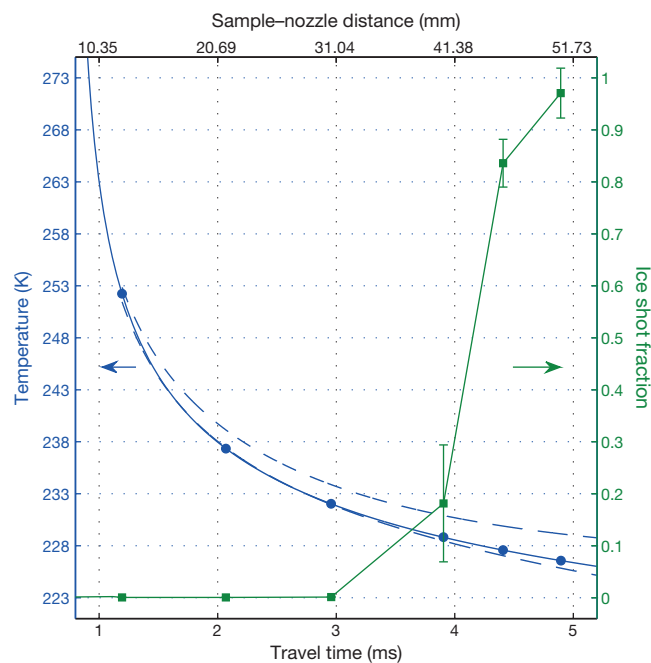


**Figure 1 | Coherent X-ray scattering from individual micrometre-sized droplets with a single-shot selection scheme. a**, A train of droplets (Supplementary Information, section A.1.1) flows in vacuum perpendicular to ~50-fs-long X-ray pulses. A coherent scattering pattern from a water droplet was recorded when a single droplet was positioned in the interaction region at the time of arrival of a single X-ray pulse. CSPAD stands for, Cornell-SLAC pixel array detector. **b, c**, Each diffraction pattern is classified (Supplementary Information, section A.1.3) either as a water shot exclusively containing pure liquid scattering characterized by a diffuse water ring (**b**), or as an ice shot characterized by intense and discrete Bragg peaks superposed on the water scattering ring (**c**).

[1]SUNCAT Center for Interface Science and Catalysis, SLAC National Accelerator Laboratory, 2575 Sand Hill Road, Menlo Park, California 94025, USA. [2]Department of Physics, AlbaNova University Center, Stockholm University, S-106 91 Stockholm, Sweden. [3]Stanford Synchrotron Radiation Lightsource, SLAC National Accelerator Laboratory, PO Box 20450, Stanford, California 94309, USA. [4]Department of Chemistry, Stanford University, Stanford, California 94305, USA. [5]PULSE Institute, SLAC National Accelerator Laboratory, 2575 Sand Hill Road, Menlo Park, California 94025, USA. [6]Center for Free-Electron Laser Science, DESY, Notkestrasse 85, 22607 Hamburg, Germany. [7]Linac Coherent Light Source, SLAC National Accelerator Laboratory, PO Box 20450, Stanford, California 94309, USA. [8]Institute for Methods and Instrumentation in Synchrotron Radiation Research, Helmholtz-Zentrum Berlin für Materialien und Energie GmbH, Wilhelm-Conrad-Röntgen Campus, Albert-Einstein-Strasse 15, 12489 Berlin, Germany. [9]Mineral Physics Institute, Stony Brook University, Stony Brook, New York, New York 11794-2100, USA.

liquid. As droplet temperature decreases, broad and bright Bragg peaks from hexagonal ice (Supplementary Information, section A.2.1) are sometimes superposed on the water scattering ring (Fig. 1c). We denote as 'water shots' diffraction patterns where we detected only water scattering, and as 'ice shots' diffraction patterns containing Bragg peaks. Ice could be detected if the illuminated volume of a droplet contained >0.05% of ice by mass (Supplementary Information, section A.2.2). For the 12-µm-diameter droplets, the number of ice shots increased drastically as the travel time exceeded ~4 ms (Fig. 2). The probing of individual water droplets with single, ultrashort X-ray pulses allowed us to separate water shots from ice shots at each temperature, to give the fraction of droplets containing ice. Even among the droplets that interacted with X-ray pulses approximately 5 ms after exiting the nozzle, with the coldest liquid temperature of $227^{+2}_{-1}$ K, we found more than 100 water shots that contained water diffraction rings and no ice diffraction peaks out of 3,600 total hits; this is below the onset temperature of ice nucleation (Fig. 2) and inside water's no man's land below $T_H \approx 232$ K at ambient pressure[13].

Structural properties of supercooled water in no-man's land can be extracted from the X-ray scattering data. The total scattering factor, $S(q)$, for each droplet temperature was obtained by averaging the scattering patterns from the respective water shots and removing the independent atomic scattering (Supplementary Information, section A.3.1). The resulting sequence of temperature-dependent $S(q)$ profiles for liquid water is shown in Fig. 3a, illustrating how the principal maximum of $S(q)$ is split into a peak $S_1$, located at $q_1 \approx 2$ Å$^{-1}$, and a peak $S_2$, located at $q_2 \approx 3$ Å$^{-1}$. The amplitudes of, and separation between, $S_1$ and $S_2$ increase with decreasing droplet temperature, indicative of an increase in structural ordering as water is supercooled ever more deeply towards and into no-man's land. Figure 3b illustrates the shift in the positions of the two peaks with temperature, as obtained from water droplets using the LCLS X-ray laser, and also based on synchrotron radiation data from metastable

liquid water at only slightly supercooled temperatures and from stable liquid water at ambient temperatures; for the latter two data sets, the temperature was measured directly. The continuous changes in the $S_1$ and $S_2$ peak positions, without apparent break when moving between the independent X-ray laser and synchrotron radiation data sets, strongly supports the temperature calibration.

At the lowest temperature accessible in the current study, the $S_1$ and $S_2$ peak positions approach the corresponding peak positions for tetrahedrally coordinated structures (Fig. 3b), represented by low-density amorphous (LDA) ice as obtained by neutron scattering[22] and modelled for clusters of hexagonal ice using kinematic scattering (Supplementary Information, section A.2.3). The rapidly increasing fraction of ice shots on the millisecond timescale below ~229 K shows that glassy water, which would be associated with slow dynamics, is not formed at these temperatures (Fig 2). We note that the continuous change in the positions of the diffraction peaks $S_1$ and $S_2$ with temperature resembles the trend of similar diffraction peaks when high-density amorphous ice transforms into LDA ice[23].

The separation between the $S_1$ and $S_2$ peaks is very sensitive to the amount and character of tetrahedrally coordinated configurations favoured by water's directional hydrogen bonds. Water exhibits a peak in the oxygen–oxygen pair-correlation function, $g_{OO}(r)$, at 4.5 Å, corresponding to the second-nearest-neighbour distance in tetrahedral coordination, $\sqrt{8/3}a$, where $a \approx 2.8$ Å is the nearest-neighbour oxygen–oxygen distance in liquid water[24]. The inset of Fig. 4a shows that increasing temperature reduces the amplitude of the second $g_{OO}(r)$ peak (henceforth denoted $g_2$) here obtained from molecular dynamics simulations using the TIP4P/2005 water model (Methods); the same trend has also been observed experimentally for an increase in pressure[25] or temperature[26]. We find that $g_2$ can be exploited as a good structural parameter to describe the
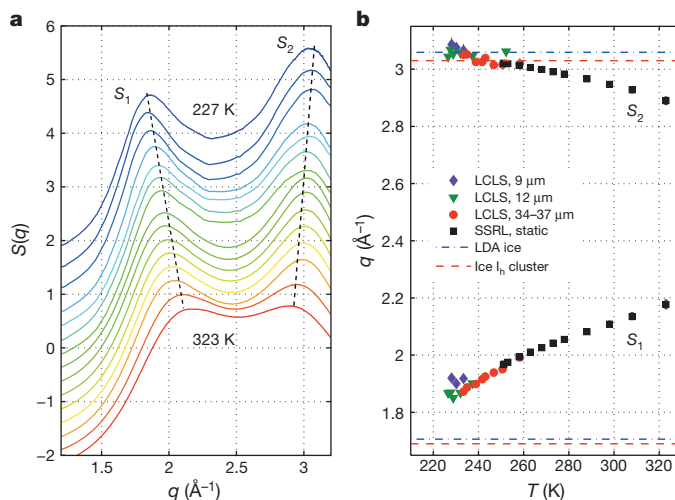


**Figure 2 | Time dependence of water crystallization during evaporative cooling.** Ice shot fraction (green) and estimated temperature (blue) as functions of travel time in vacuum for droplets of diameter 12 µm and speed 10.35 m s$^{-1}$. From the ice shot fraction, shown as mean ± s.d. of two to seven individual recordings, we find the onset of ice nucleation to lie between $232^{+2}_{-0.1}$ and $229^{+2}_{-1}$ K. The dashed blue lines represent maximum and minimum temperatures from the Knudsen model, which consistently overlap with experimental data sets from SSRL measured at known absolute temperatures (Supplementary Information, sections A.3.2 and B.3.5).



**Figure 3 | Temperature dependence of water scattering peaks. a,** Scattering structure factor, $S(q)$, obtained from single-shot diffraction patterns (Supplementary Information, section A.3.1). Water temperature decreases from bottom to top (SSRL: 323, 298, 273, 268, 263, 258, 253, 251 K; LCLS: 251, 247, 243, 239, 232, 229, 227 K). The data reveal a split of the principal $S(q)$ maximum into two well-separated peaks, $S_1$ and $S_2$ (dashed lines). **b,** Temperature dependence of the $S_1$ and $S_2$ peak positions, calculated from the maxima of local fifth-order polynomial least-squares fits with error bars estimated by shifting the derivatives of the polynomial fits by ±0.05 Å (LCLS) and ±0.15 Å (SSRL) (Supplementary Information, section A.3.1). Green triangles are LCLS data from 12-µm-diameter droplets; red circles are LCLS data from 34- and 37-µm-diameter droplets; and black squares are SSRL data from a static liquid sample. Purple diamonds are LCLS data from 9-µm-diameter droplets measured at a separate LCLS run with separate $q$-calibration (Supplementary Information, section A.1.2). As the temperature decreases in no man's land, the positions of peaks $S_1$ and $S_2$ approach the characteristic values of LDA ice (dash–dot blue lines) as determined from neutron diffraction[22] and clusters of hexagonal ice (ice $I_h$; dashed red lines; Supplementary Information, section A.2.3).
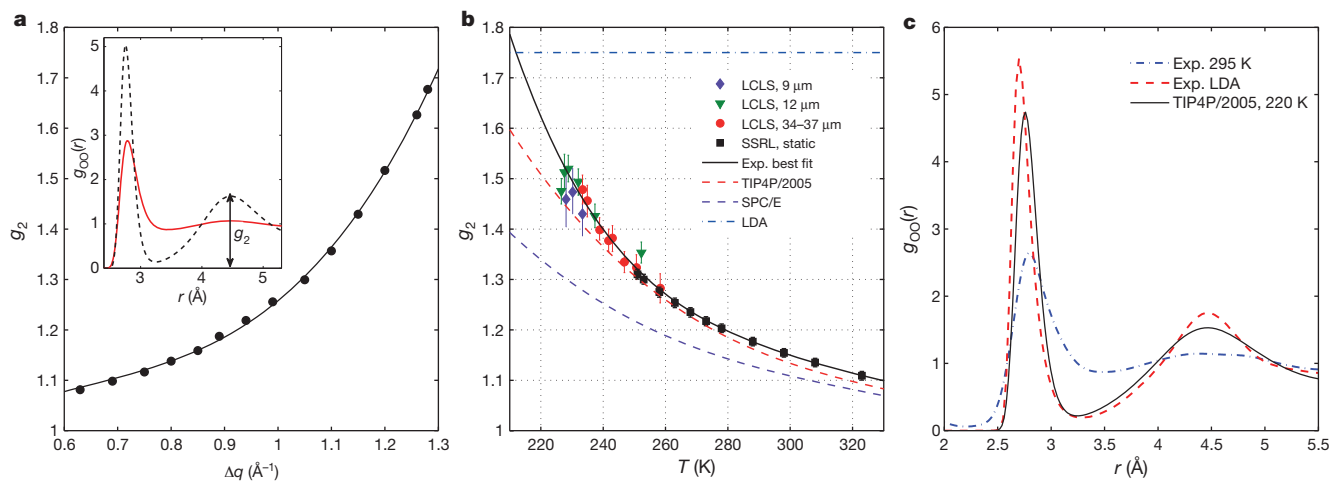
**Figure 4 | Temperature dependence of the tetrahedrality of liquid water.**
**a**, Magnitude of the second $g(r)$ peak, $g_2$, as a function of the splitting, $\Delta q$, between the $S_1$ and $S_2$ peaks from TIP4P/2005 molecular dynamics simulations (dots). The inset illustrates $g_2$ for $g(r)$ at 340 K (red solid line) and 210 K (black dashed line). **b**, Experimental $g_2$ values, derived from measured $\Delta q$ values (labels as in Fig. 3b) and the fit to molecular dynamics data shown in **a**, with error bars estimated from the maximum and minimum $\Delta q$ values allowed by the uncertainty in the $S_1$ and $S_2$ peak positions. Also shown is the fourth-order polynomial least-squares fit to the experimental data (black solid line), where the last (that is, low-$T$) two data points for the 12-μm-diameter droplets

and the last data point for the 9-μm-diameter droplets are ignored owing to high nonlinearity in the detector response, which artificially decreases $g_2$ (Supplementary Information, section A.3.1). For comparison, the temperature dependences of $g_2$ for the TIP4P/2005 (red dashed line) and SPC/E (purple dashed line) models are depicted along with the characteristic value of $g_2$ for LDA ice[22] (blue dash–dot line). **c**, The $g(r)$ of TIP4P/2005 water at 220 K (black solid line) bears a striking similarity to LDA ice[22] (red dashed line), whereas the measured $g(r)$ of room-temperature water[24] (blue dash–dot line) shows significantly less structural correlation.

tetrahedrality of liquid water, as demonstrated by the similar temperature dependences of $g_2$ and the tetrahedrality, $Q$, commonly used in molecular dynamics simulations[27] (Supplementary Fig. 21). The molecular dynamics simulations furthermore show a clear correlation between $g_2$ and the splitting, $\Delta q = q_2 - q_1$, between the $S_1$ and $S_2$ peaks, where $g_2$ increases monotonically with $\Delta q$ (Fig. 4a). We make use of this relationship to extract from the measured $\Delta q$ data 'experimental' $g_2$ values, which are plotted against temperature in Fig. 4b and compared with $g_2$ values from molecular dynamics simulations using the TIP4P/2005 and SPC/E water models.

The data in Fig. 4b show that as water is cooled from above its freezing temperature, $g_2$ and its rate of change increase continuously as would be expected from the accelerated growth of tetrahedral structures in deeply supercooled water. We also note that the best-fit extrapolation of $g_2$ to low temperatures approaches the limit for LDA ice[22] (dash–dot line in Fig. 4b), which is expected to be representative also of crystalline hexagonal ice (Fig. 3b), although $g_2$ cannot be uniquely defined for a crystalline sample. Furthermore, $g_{OO}(r)$ for LDA ice and simulated supercooled TIP4P/2005 water at 220 K—with the same $g_2$ value as the maximum in the experimental data—are very similar, but differ from $g_{OO}(r)$ for water at ambient conditions (Fig. 4c). The structure of liquid water in no man's land is therefore distinct from that of water under ambient conditions, exhibiting stronger tetrahedral ordering. The largest $g_2$ values obtained from the experimental data (Fig. 4b) coincide with the observed onset of ice nucleation at ~229 K (Fig. 2), supporting simulations[10,28] which concluded that the increased abundance and persistence of tetrahedrally coordinated water molecules play a central part as precursor structure for homogeneous ice nucleation.

We still observe a non-negligible number of water shots at the farthest measurement point, reached about 1 ms after the temperature of the corresponding water droplet has dropped to $229^{+2}_{-1}$ K, where homogeneous nucleation sets in (Fig. 2). This implies that metastable water can transiently exist on the millisecond timescale down to $227^{+2}_{-1}$ K. We expect that these observations and our data mapping the structural evolution of supercooled liquid water with decreasing temperature (Extended Data Tables 1–4) will enable a quantitative evaluation of different theoretical models that predict this structure in no man's land and aim to explain water's anomalous physical properties.

## METHODS SUMMARY

Deionized water (PURELAB Ultra Genetic; resistivity 18.2 MΩ cm at 298 K) was measured at the Stanford Synchrotron Radiation Lightsource (SSRL) small-angle X-ray scattering instrument (beam line 4-2) in a static, ~5-μl sample cell with an absolute temperature uncertainty of ±1 K. The experimental details have been described elsewhere[2]. X-ray scattering experiments on water droplets of diameters 9, 12, 34 and 37 μm were performed using the LCLS coherent X-ray imaging instrument[29] on deep supercooling (<260 K) calibrated according to the Knudsen theory of evaporation (Supplementary Information, section B3). These measurements overlap with those made at SSRL (>250 K). Molecular dynamics simulations of evaporative cooling of 1–4-nm-radii droplets were performed using the TIP4P/2005 force field to verify the Knudsen theory of evaporation (Supplementary Information, section B2). The single-pulse water scattering patterns at LCLS were recorded with the Cornell-SLAC pixel array detector and corrected for the dark signal, gain variations, the polarization dependence of the X-ray scattering, solid-angle differences and fluctuations in the average photon wavelength between X-ray pulses (Supplementary Information, section A.1.2). More details on the procedure for selecting water shots and sample statistics are given in Supplementary Information, section A.1.3. The total scattering structure factor was obtained from the averaged angularly integrated intensities by removing the atomic form factor contribution (Supplementary Information, section A.3.1). Measurements from both SSRL and LCLS had a scattering momentum transfer range of approximately $0.5\ \text{Å}^{-1} \le q \le 3.5\ \text{Å}^{-1}$. Large-scale (45,000 molecules) molecular dynamics simulations[30] of bulk TIP4P/2005 water and medium-scale (512 molecules) molecular dynamics simulations of SPC/E water were performed for a wide range of temperatures to calculate the total scattering structure factor (Supplementary Information, section C.1.1), including intermolecular oxygen–hydrogen and oxygen–oxygen partial structure factors and the intramolecular oxygen–hydrogen partial structure factor (the hydrogen–hydrogen contribution is negligible), which were used for the calibration of $g_2$ against $\Delta q$ (Supplementary Information, section C.1.3).

1. Speedy, R. J. & Angell, C. A. Isothermal compressibility of supercooled water and evidence for a thermodynamic singularity at −45°C. *J. Chem. Phys.* **65**, 851–858 (1976).
2. Huang, C. *et al.* Increasing correlation length in bulk supercooled H₂O, D₂O, and NaCl solution determined from small angle X-ray scattering. *J. Chem. Phys.* **133**, 134504 (2010).

3. Angell, C. A., Sichina, W. J. & Oguni, M. Heat capacity of water at extremes of supercooling and superheating. *J. Phys. Chem.* **86,** 998–1002 (1982).
4. Poole, P. H., Sciortino, F., Essmann, U. & Stanley, H. E. Phase behaviour of metastable water. *Nature* **360,** 324–328 (1992).
5. Sastry, S., Debenedetti, P. G., Sciortino, F. & Stanley, H. E. Singularity-free interpretation of the thermodynamics of supercooled water. *Phys. Rev. E* **53,** 6144–6154 (1996).
6. Angell, C. A. Insights into phases of liquid water from study of its unusual glass-forming properties. *Science* **319,** 582–587 (2008).
7. Limmer, D. T. & Chandler, D. The putative liquid-liquid transition is a liquid-solid transition in atomistic models of water. *J. Chem. Phys.* **135,** 134503 (2011).
8. Palmer, J. C., Car, R. & Debenedetti, P. G. The liquid-liquid transition in supercooled ST2 water: a comparison between umbrella sampling and well-tempered metadynamics. *Faraday Discuss.* **167,** 77–94 (2013).
9. Speedy, R. J. Stability-limit conjecture. An interpretation of the properties of water. *J. Phys. Chem.* **86,** 982–991 (1982).
10. Moore, E. B. & Molinero, V. Structural transformation in supercooled water controls the crystallization rate of ice. *Nature* **479,** 506–508 (2011).
11. Holten, V. & Anisimov, M. A. Entropy-driven liquid–liquid separation in supercooled water. *Sci. Rep.* **2,** 713 (2012).
12. Overduin, S. D. & Patey, G. N. An analysis of fluctuations in supercooled TIP4P/2005 water. *J. Chem. Phys.* **138,** 184502 (2013).
13. Mason, B. J. The supercooling and nucleation of water. *Adv. Phys.* **7,** 221–234 (1958).
14. Smith, R. S. & Kay, B. D. The existence of supercooled liquid water at 150 K. *Nature* **398,** 788–791 (1999).
15. Neuefeind, J., Benmore, C. J., Weber, J. K. R. & Paschek, D. More accurate X-ray scattering data of deeply supercooled bulk liquid water. *Mol. Phys.* **109,** 279–288 (2011).
16. Mallamace, F., Corsaro, C., Baglioni, P., Fratini, E. & Chen, S.-H. The dynamical crossover phenomenon in bulk water, confined water and protein hydration water. *J. Phys. Condens. Matter* **24,** 064103 (2012).
17. Manka, A. *et al.* Freezing water in no-man's land. *Phys. Chem. Chem. Phys.* **14,** 4505–4516 (2012).
18. Levinger, N. E. Water in confinement. *Science* **298,** 1722–1723 (2002).
19. Faubel, M., Schlemmer, S. & Toennies, J. P. A molecular beam study of the evaporation of water from a liquid jet. *Z. Phys. D* **10,** 269–277 (1988).
20. Rayleigh, F. R. S. On the instability of jets. *Proc. Lond. Math. Soc.* **10,** 4–12 (1879).
21. DePonte, D. P. *et al.* Gas dynamic virtual nozzle for generation of microscopic droplet streams. *J. Phys. D Appl. Phys.* **41,** 195505 (2008).
22. Bowron, D. T. *et al.* The local and intermediate range structures of the five amorphous ices at 80 K and ambient pressure: a Faber-Ziman and Bhatia-Thornton analysis. *J. Chem. Phys.* **125,** 194502 (2006).
23. Tulk, C. A. *et al.* Structural studies of several distinct metastable forms of amorphous ice. *Science* **297,** 1320–1323 (2002).
24. Skinner, L. B. *et al.* Benchmark oxygen-oxygen pair-distribution function of ambient water from x-ray diffraction measurements with a wide Q-range. *J. Chem. Phys.* **138,** 074506 (2013).
25. Okhulkov, A. V., Demianets, Y. N. & Gorbaty, Y. E. X-ray scattering in liquid water at pressures of up to 7.7 kbar: test of a fluctuation model. *J. Chem. Phys.* **100,** 1578–1588 (1994).
26. Narten, A. H., Danford, M. D. & Levy, H. A. X-ray diffraction study of liquid water in temperature range 4–200 °C. *Discuss. Faraday Soc.* **43,** 97–107 (1967).
27. Errington, J. R. & Debenedetti, P. G. Relationship between structural order and the anomalies of liquid water. *Nature* **409,** 318–321 (2001).
28. Matsumoto, M., Saito, S. & Ohmine, I. Molecular dynamics simulation of the ice nucleation and growth process leading to water freezing. *Nature* **416,** 409–413 (2002).
29. Boutet, S. & Williams, G. J. The coherent X-ray imaging (CXI) instrument at the Linac Coherent Light Source (LCLS). *New J. Phys.* **12,** 035024 (2010).
30. Wikfeldt, K. T., Huang, C., Nilsson, A. & Pettersson, L. G. M. Enhanced small-angle scattering connected to the Widom line in simulations of supercooled water. *J. Chem. Phys.* **134,** 214506 (2011).

**Author Contributions** A.N., C.H. and M.J.B. had the idea for and designed the experiment; S.B., G.J.W., M.M. and M.M.S. operated the coherent X-ray imaging instrument; M.J.B., D.P.D., T.A.M., J.A.S., C.H., R.G.S., C.Y.H., H.L. and D. Starodub developed, tested and ran the sample delivery system; C.H., T.A.M. and T.M.W. performed the SSRL experiment; J.A.S., T.A.M., H.L., R.G.S., C.H., D.N., M.B., D.P.D., D. Starodub, C.Y.H., C. Chen, L.B.S., M.M.S., M.M., G.J.W., S.B., M.J.B. and A.N. performed the LCLS experiments; A.B., J.A.S., N.D.L., A.V.M., G.J.W. and C. Caronna developed data processing software; J.A.S., C.H., N.D.L., H.L., D.N., A.V.M. and J.F. processed, sorted and analysed data; D. Schlesinger, K.T.W. and L.G.M.P. designed and performed the molecular dynamics simulations; D. Schlesinger, J.A.S., C.H., T.A.M., D. Starodub and L.G.M.P. implemented and simulated the Knudsen theory of evaporation; and A.N., C.H., L.G.M.P., J.A.S., D. Schlesinger and N.D.L. wrote the manuscript with input from all authors.

**Author Information** Reprints and permissions information is available at www.nature.com/reprints. The authors declare no competing financial interests. Readers are welcome to comment on the online version of the paper. Correspondence and requests for materials should be addressed to J.A.S. (sellberg@slac.stanford.edu) or A.N. (nilsson@slac.stanford.edu).

**Extended Data Table 1 | Temperature-dependent $S_1$ and $S_2$ peak positions for the 5-μl static sample**

| Temperature (K) | $q_1$ (Å$^{-1}$) | $q_2$ (Å$^{-1}$) |
|---|---|---|
| 323 ± 1 | 2.177 ± 0.016 | 2.890 ± 0.014 |
| 308 ± 1 | 2.135 ± 0.013 | 2.928 ± 0.011 |
| 298 ± 1 | 2.108 ± 0.011 | 2.947 ± 0.009 |
| 288 ± 1 | 2.082 ± 0.009 | 2.966 ± 0.007 |
| 278 ± 1 | 2.055 ± 0.007 | 2.983 ± 0.006 |
| 273 ± 1 | 2.042 ± 0.007 | 2.991 ± 0.006 |
| 268 ± 1 | 2.026 ± 0.007 | 2.999 ± 0.006 |
| 263 ± 1 | 2.011 ± 0.006 | 3.006 ± 0.005 |
| 258 ± 1 | 1.994 ± 0.006 | 3.013 ± 0.005 |
| 253 ± 1 | 1.975 ± 0.006 | 3.019 ± 0.004 |
| 251 ± 1 | 1.967 ± 0.005 | 3.021 ± 0.004 |

The temperature-dependent $S_1$ and $S_2$ peak positions, respectively $q_1$ and $q_2$, derived from the maxima of local (fifth-order) polynomial least-squares fits for the 5-μl static sample measured at beamline 4-2 at SSRL in January 2012. The error bars for the temperature correspond to the measurement accuracy (IEC 584-2 standard for K-type thermocouples); the error bars for $q_1$ and $q_2$ were estimated by shifting the derivatives of the polynomial fits by ±0.15 Å when determining the positions of the maxima (Supplementary Information, section A.3.1).

**Extended Data Table 2 | Temperature-dependent $S_1$ and $S_2$ peak positions for the 34–37-μm-diameter droplets**

| Temperature (K) | $q_1$ (Å⁻¹) | $q_2$ (Å⁻¹) |
|---|---|---|
| $258\,^{+5}_{-3}$ | 1.992 ± 0.011 | 3.019 ± 0.021 |
| $251\,^{+3}_{-2}$ | 1.950 ± 0.008 | 3.016 ± 0.014 |
| $247\,^{+2}_{-1}$ | 1.939 ± 0.008 | 3.015 ± 0.011 |
| 243 ± 2 | 1.925 ± 0.008 | 3.039 ± 0.013 |
| 242 ± 1 | 1.915 ± 0.006 | 3.025 ± 0.011 |
| 239 ± 1 | 1.899 ± 0.006 | 3.025 ± 0.011 |
| $235\,^{+1}_{-2}$ | 1.887 ± 0.008 | 3.052 ± 0.013 |
| 233 ± 1 | 1.872 ± 0.007 | 3.051 ± 0.011 |

The temperature-dependent $S_1$ and $S_2$ peak positions, respectively $q_1$ and $q_2$, derived from the maxima of local (fifth-order) polynomial least-squares fits for the 34–37-μm-diameter droplets measured using the coherent X-ray imaging (CXI) instrument at LCLS in February 2011. The error bars for the temperature were estimated by forcing overlap between experimental data sets using the Knudsen theory of evaporation (Supplementary Information, section B.3.5); the error bars for $q_1$ and $q_2$ were estimated by shifting the derivatives of the polynomial fits by ±0.05 Å when determining the positions of the maxima (Supplementary Information, section A.3.1).

**Extended Data Table 3 | Temperature-dependent $S_1$ and $S_2$ peak positions for the 12-μm-diameter droplets**

| Temperature (K) | $q_1$ (Å$^{-1}$) | $q_2$ (Å$^{-1}$) |
|---|---|---|
| 252 $^{+2}_{-1}$ | 1.971 ± 0.009 | 3.062 ± 0.008 |
| 237 $^{+2}_{-0.2}$ | 1.901 ± 0.006 | 3.046 ± 0.010 |
| 232 $^{+2}_{-0.1}$ | 1.868 ± 0.006 | 3.056 ± 0.010 |
| 229 $^{+2}_{-1}$ | 1.850 ± 0.005 | 3.053 ± 0.010 |
| 228 $^{+2}_{-1}$ | 1.869 ± 0.008 | 3.068 ± 0.013 |
| 227 $^{+2}_{-1}$ | 1.867 ± 0.006 | 3.044 ± 0.010 |

The temperature-dependent $S_1$ and $S_2$ peak positions, respectively $q_1$ and $q_2$, derived from the maxima of local (fifth-order) polynomial least-squares fits for the 12-μm-diameter droplets measured using the CXI instrument at LCLS in February 2011. The error bars for the temperature were estimated by forcing overlap between experimental data sets using the Knudsen theory of evaporation (Supplementary Information, section B.3.5); the error bars for $q_1$ and $q_2$ were estimated by shifting the derivatives of the polynomial fits by ±0.05 Å when determining the positions of the maxima (Supplementary Information, section A.3.1).

**Extended Data Table 4 | Temperature-dependent $S_1$ and $S_2$ peak positions for the 9-μm-diameter droplets**

| Temperature (K) | $q_1$ (Å⁻¹) | $q_2$ (Å⁻¹) |
|---|---|---|
| $233\ ^{+2}_{-1}$ | 1.918 ± 0.010 | 3.066 ± 0.022 |
| $230\ ^{+2}_{-1}$ | 1.900 ± 0.009 | 3.076 ± 0.019 |
| $228\ ^{+2}_{-1}$ | 1.920 ± 0.013 | 3.087 ± 0.024 |

The temperature-dependent $S_1$ and $S_2$ peak positions, respectively $q_1$ and $q_2$, derived from the maxima of local (fifth-order) polynomial least-squares fits for the 9-μm-diameter droplets measured using the CXI instrument at LCLS in January 2013. The error bars for the temperature were estimated by forcing overlap between experimental data sets using the Knudsen theory of evaporation (Supplementary Information, section B.3.5); the error bars for $q_1$ and $q_2$ were estimated by shifting the derivatives of the polynomial fits by ±0.05 Å when determining the positions of the maxima (Supplementary Information, section A.3.1).